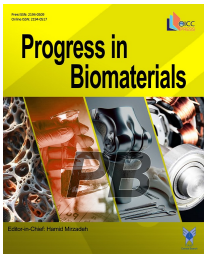

Volume 13, Issue 2, 132406 (1-18)

Progress in Biomaterials (PIBM)

https://doi.org/10.57647/pibm.2024.132406

Evaluation of Morphology, Degradation, and Biocompatibility of Fluorideapatite–Bioactive Glass (453P4) Nanocomposites

Fatemeh Mirjalili[1,*], Sahebali Manafi[2]

[1]*Department of Materials Engineering, May.C., Branch, Islamic Azad University, Maybod, Iran.*
[2]*Department of Materials Engineering, Sha.C., Islamic Azad University, Shahrood, Iran.*

[*]**Corresponding author:** f.mirjalili1404 @iau.ir

Original Research

Abstract:

Bioceramic nanocomposites are increasingly explored for bone regeneration and dental applications due to their tunable bioactivity and mechanical properties. This study investigates the physicochemical properties, degradation behavior, bioactivity, mechanical performance, cytocompatibility, and antibacterial activity of fluorapatite-based nanocomposite ceramics reinforced with 10, 20, and 30 wt.% of S53P4 bioglass synthesized via the sol-gel method. The composites were characterized for degradation by monitoring weight loss and pH changes, while bioactivity was assessed through apatite layer formation in simulated body fluid (SBF). The release of silicon and fluoride ions was quantified using inductively coupled plasma spectroscopy and a fluoride-selective electrode, respectively. Cytocompatibility was examined via MTT assay on osteoblast-like cells over 1 to 7 days. Antibacterial activity was assessed against Streptococcus mutans using colony count reduction. Results showed that, increasing the S53P4 content enhanced degradation and bioactivity, reflected in higher ion release and more significant apatite formation, while compressive strength increased proportionally with the bioglass content. MTT assays demonstrated favorable cytocompatibility, with no evidence of cytotoxicity, although cell viability slightly decreased after 7 days compared to day 1. Antibacterial tests confirmed a reduction in S. mutans colonies with higher glass phase percentages, indicating improved antibacterial potential. These findings highlight the potential of fluorapatite–S53P4 nanocomposites as promising biomaterials for bone regeneration and dental applications.

Keywords:

Fluorapatite; S53P4 bioglass; Nano-composite; Bioactivity; Apatite layer formation; Antibacterial properties

Cite this article: Mirjalili, F., Manafi, S. Evaluation of Morphology, Degradation, and Biocompatibility of Fluorideapatite–Bioactive Glass (453P4) Nanocomposites *Progress in Biomaterials* **13**(2), Article 06 (2024).

1. Introduction

Bone is a living connective tissue that not only provides structural stability for the human body but also acts as a dynamic calcium reservoir during both physiological remodeling and pathological repair (Florencio-Silva et al., 2015; Clarke, 2008). Approximately 65 – 70 wt.% of bone consists of biological hydroxyapatite (HA), reflecting the intricate interplay of organic and inorganic phases that inspires biomimetic approaches in bone tissue engineering (Kazimierczak et al., 2023; Dorozhkin, 2009). Bioceramics are widely employed in clinical practice as substitutes for compromised bone, functioning as load-bearing fillers, coatings, or drug delivery systems (Aoba and Fejerskov, 2002; Pandayil et al., 2024; Rezwan et al., 2006). Among them, calcium phosphate ceramics, especially HA, and bioactive glasses (BGs) are considered the most promising due to their high biocompatibility and osteoconductivity (Shearer et al., 2023; Montazerian et al., 2022; Ielo et al., 2022). Incorporation of bioactive glass(BG) particles into HA matrices enhances mechanical properties and bioactivity, owing to controlled ion release and improved protein adsorption (Elliott et al., 1973; Välimäki and Aro, 2006). Fluoride substitution in the HA lattice further improves stability and osteogenic response. Replacing hydroxyl groups (OH^-) with fluoride ions (F^-) yields fluorapatite (FA, $Ca_{10}(PO_4)_6F_2$), which exhibits higher chemical durability, lower solubility, and superior osteoconductivity than stoichiometric HA (Brudevold et al., 1956; Ten Cate, 1999; Weatherell JA, 1986). This is physiologically relevant, given that cortical bone contains $\sim$ 1 wt.% fluoride, which contributes to maintain-

ing bone density and preventing osteoporosis (Featherstone, 1999; Weatherell et al., 1986; Buzalaf et al., 2011; Nielson et al., 2024). Moreover, FA naturally constitutes the enamel of teeth, where partial OH^- substitution with F^- enhances resistance to acidic degradation (Brudevold et al., 1956; Ten Cate, 1999; Weatherell JA, 1986; Borkowski et al., 2023; Elliott, 2023). Nevertheless, the intrinsic brittleness and low fracture toughness of FA continue to limit its suitability for load-bearing applications (Nielson et al., 2024; Santiago et al., 2022). To overcome these constraints, silicate-based bioactive glasses particularly S53P4 and the newer 453P4 formulation have gained significant attention due to their enhanced mechanical resilience, high bioactivity, and intrinsic antibacterial behavior arising from alkali-ion release and localized pH elevation (Kargozar et al., 2018; Brauer, 2015; Kaou et al., 2023a). Among these, BG 45S5, first introduced by Hench in 1969 (Hench and Wilson, 2013; Jones, 2013), remains a historical benchmark owing to its exceptionally high in vivo bioactivity index (IB > 8), which surpasses that of most bioceramics (Drevet et al., 2024; Bigoni et al., 2019; Rahaman et al., 2011). Recent evidence has highlighted the antimicrobial and osteogenic dual functionality of S53P4, with successful outcomes reported in craniofacial reconstruction and the treatment of osteomyelitis (Lindfors et al., 2017). Parallel advances suggest the promising synergy achievable in FA–BG hybrid systems. Manafi et al. showed that, integrating FA into BG frameworks modulates degradation kinetics while enabling controlled fluoride release (Manafi et al., 2019b; Manafi et al., 2019a). Additional studies have confirmed that, FA-BG scaffolds accelerate in vivo bone formation and enhance trabecular integration without eliciting foreign-body reactions (Xuan et al., 2024). Despite these advances, comprehensive analyses of FA–BG composites produced via sol–gel or gel-casting methods particularly those incorporating emerging glass compositions such as 453P4 remain limited (Xuan et al., 2024; Seyedmajidi et al., 2023; van Gestel et al., 2015). Given this gap, S53P4 was selected for the present study due to its balanced combination of bioactivity, controlled dissolution behavior, and clinically validated antibacterial efficacy. Compared with 45S5 Bioglass, which dissolves rapidly and exhibits reduced thermal stability, S53P4 ensures more sustained ion release and improved structural reliability. Furthermore, unlike slower-degrading systems such as 13-93, S53P4 forms hydroxycarbonate apatite more rapidly and provides stronger osteostimulatory cues. This intermediate yet synergistically advantageous profile makes S53P4 an optimal candidate for designing FA–BG nanocomposites with enhanced osteogenic potential and improved scaffold performance (Kaou et al., 2023b).

This study uniquely presents a sol–gel synthesized fluorapatite (FA)–S53P4 bioactive glass nanocomposite, a combination that remains scarcely explored compared to the extensively investigated hydroxyapatite (HA) bioactive glass systems.Fluorapatite, with its enhanced chemical stability, controlled fluoride release, and slower degradation rate, offers superior structural properties and potential for stimulating bone density and enamel integrity but has been limited by intrinsic brittleness (Brudevold et al., 1956; Ten Cate, 1999; Weatherell JA, 1986; Featherstone, 1999; Weatherell et al., 1986; Buzalaf et al., 2011; Nielson et al., 2024; Borkowski et al., 2023; LeGeros, 2002). S53P4 bioactive glass, on the other hand, is clinically celebrated for its strong osteoconductivity, antibacterial capacity, and ion-mediated bioactivity even against resistant pathogens-though its mechanical limitations hinder broader structural use (Gorustovich et al., 2021; Kondo et al., 2024; Ylänen, 2017; Hoppe et al., 2011; Gatti et al., 2024). By integrating FA as a chemically robust matrix and S53P4 as an active biofunctional phase, this research establishes a synergistic nanocomposite system. Critically, it examines compositional tuning across 10, 20, and 30 wt.% S53P4, and systematically evaluates degradation (weight loss, pH changes), ion release (Si and F), bioactivity (apatite layer formation), cytocompatibility (via MTT assay), and antibacterial efficacy against Streptococcus mutans.This work fills an important gap by delivering a multifunctional FA–S53P4 nanocomposite with optimized degradation, bioactivity, mechanical stability, and antibacterial action, offering significant promise for advanced bone regeneration and dental restorative applications.

2. Experimental procedures

2.1 Preparation of fluorapatite- S53P4 bioglass composite powder

For synthesis of bioactive glasses of S53P4-fluorapatite nanocomposites with 10, 20 and 30 wt.% of bioactive glasses, two sols of bioactive glass and fluorapatite were prepared. At first, 5.91 g of calcium nitrate of tetrahydrate ($Ca(NO_3)_2 \cdot 4H_2O$, 98%, Merck, CN) in 20 mL of ethanol (98%, Merck, ET)/water (W) solution (75-25%) was dissolved. Then, 1.36 g triethyl phosphate (99%, Merck, TP) in 20 mL of ET/W solution (75-25%) was stirred for 1 h. At the same time, 0.28 g ammonium fluoride (98%, Merck, AF) precursor in 20 mL of ET/W solution (75-25%) was dissolved and stirred at 45 °C. Then, at first, hydrolysis of 22.48 mL of tetraethoxysilane (TEOS) in 350 mL of distilled water and 350 mL of ethanol at room temperature and formerly, adjusted of pH at 2 by nitric acid with continuous stirring for 1 h. Therefore, the addition of 8.97 g of calcium nitrate hydrate to the above solution and continues stirring until dissolving. After that, addition of 1.55 g of $NaNO_3$ to the above mixture (the previous mixture was named solution A) and then, 3.34 g of ammonium dihydrogen phosphate was added to the distilled water (this mixture was named solution B). Furthermore, solution (B) was gradually added on solution (A) with continuous stirring for overnight.

The two precursor sols were subsequently combined and magnetically stirred for 2 h to ensure homogeneous mixing. The resulting mixtures were then kept at ambient temperature for 14 days, during which their pH remained within $7.6 - 8.6$, allowing each composition prepared at different weight ratios to gradually transform into a uniform, transparent gel. The matured gels were freeze-dried under controlled conditions (−51 °C, 0.5 torr, 48 h) to remove residual solvents without structural collapse. The obtained dried gels were finally calcined at 600 °C for 1 h to yield fine fluorapatite -S53P4 bioglass nanocomposite powders. A schematic overview of the synthesis procedure and the

coding of the prepared samples are provided in Fig. 1 and Table 1, respectively.

2.2 Characterization of samples

2.2.1 Phase analysis and morphological properties

Phase analysis of the samples was conducted using a Siemens D-500 X-ray diffractometer with a Cu-Kα radiation source ($\lambda = 1.5406$ Å). Data were collected over a 2θ range of 20–70° with a step size of 0.02° and a scanning speed of 2°/min. The instrument was operated at 40 kV and 30 mA. The crystallinity of the nanocomposites was evaluated using both the Landi equation and the Scherrer equation based on XRD patterns to ensure accuracy in the estimation of crystalline content. The morphological of the sintered powders were recognized by field emission scanning electron microscope (FESEM, HitachiSU8700, Japan).

2.2.2 Preparation of simulated body fluid (SBF)

Simulated body fluid (SBF) was prepared according to a modified Kokubo protocol. Briefly, 700 mL of deionized water was placed in a water bath and heated to ~ 36 °C. Under continuous stirring, the following reagents were added sequentially to ensure complete dissolution: sodium chloride (NaCl), sodium bicarbonate ($NaHCO_3$), potassium chloride (KCl), potassium hydrogen phosphate trihydrate ($K_2HPO_4 \cdot 3H_2O$), magnesium chloride hexahydrate ($MgCl_2 \cdot 6H_2O$), 1 M hydrochloric acid (HCl), calcium chloride ($CaCl_2$), and sodium sulfate (Na_2SO_4). Pre-heated deionized water was then added to adjust the total volume

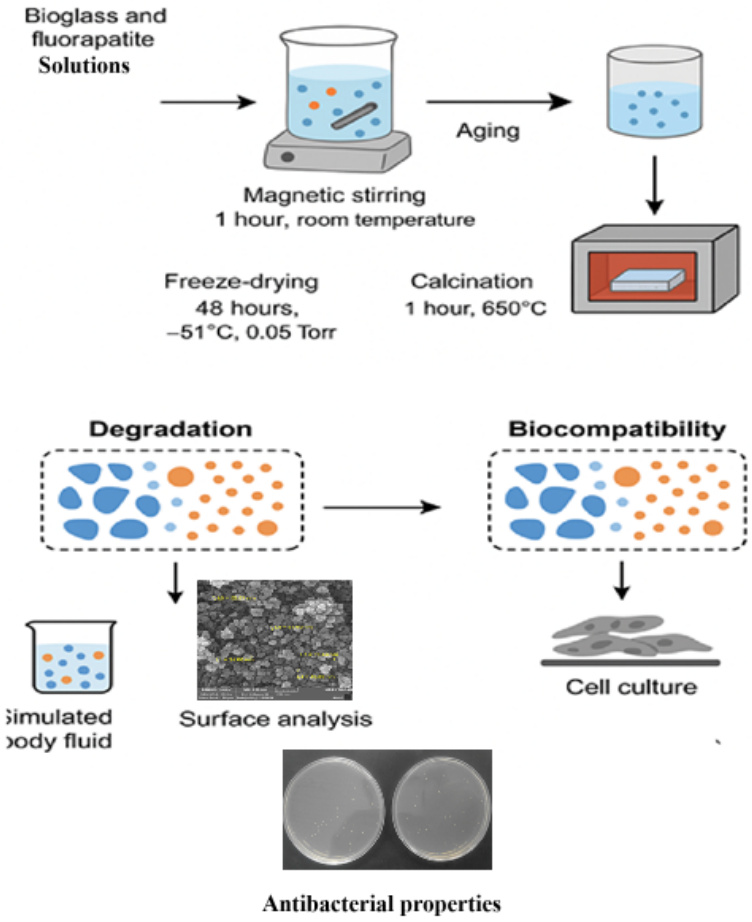

Figure 1. Schematic illustration of fluorapatite- S53P4 nano composite preparation.

Table 1. The code of samples.

Code	Sample
FA	Fluorapatite of 100(wt.%)
FA-BG-10	Fluorapatite– S53P4 bioglass 10(wt.%)
FA-BG-20	Fluorapatite– S53P4 bioglass 20(wt.%)
FA-BG-30	Fluorapatite– S53P4 bioglass 30(wt.%)
BG	S53P4 bioglass of 100(wt.%)

to 900 mL while maintaining the solution temperature at $\sim$ 36 °C, resulting in a pH below 2. The pH was subsequently adjusted to 7.45 $\pm$ 0.02 by the controlled addition of a 1 M NaOH. Finally, while maintaining the solution temperature at 36 $\pm$ 0.5 °C, the total volume was adjusted to 1000 mL with deionized water, yielding an SBF with ionic composition comparable to that of human blood plasma (Kokubo and Takadama, 2006).

2.2.3 Biodegradability test

To determine the external properties of the nanocomposites, the synthesized powders are immersed in a simulated fluid in different time intervals. The synthesized nanopowders and the simulant solution are mixed with 1 mg/mL ratio and then placed on the shaker at 37 °C. The process is to approve that the samples are stored in the solution for a definite period, during which it changes. The sample is then dried at 50 °C and subjected to the additional measurements. For the purpose of the study, the biodegradability and bioactivity of the gained samples are measured by different parameters such as a change in the pH and the weight which can be calculated according to the equation (1)

$$\text{Weight loss}(\%) = \frac{M_{bi} - M_{af}}{M_{af}} \times 100 \tag{1}$$

where M_{bi} is the initial weight and M_{af} is the weight after immersion (Rahaman et al., 2011; Lindfors et al., 2017).

2.2.4 Inductively coupled plasma

Elemental analysis and quantification of released ions were performed using an Inductively Coupled Plasma Optical Emission Spectrometer (ICP-OES, PerkinElmer Optima 8000, USA).
Inductively coupled plasma spectroscopy is one of the atomic spectroscopy methods in which the atomization of elements is carried out with the help of a warm plasma environment. This method is more sensitive than other methods, with better detection limits and higher reproducibility.

2.2.5 Fluoride ion-selective electrode

The concentration of released fluoride ions from fluorinated samples was determined using a fluoride ion-selective electrode (Fluoride ISE, Metrohm) in a simulated solution. The fluoride ion-selective electrode operates based on a potentiometric principle, whereby the electrical potential difference developed across a selective membrane in response to fluoride ion activity is measured relative to a reference electrode (typically Ag/AgCl). The measured potential is related to the fluoride ion activity according to the Nernst equation, rather than to a direct flow or accumulation of electrical charge. Accordingly, the formation and evolution of the apatite layer on the immersed samples were evaluated using scanning electron microscopy (SEM) to examine surface morphology and energy-dispersive X-ray spectroscopy (EDS) to assess elemental composition.

2.2.6 Evaluation of cell survival by MTT (3-(4,5-Dimethylthiazol-2-Yl)-2,5-Diphenyltetrazolium Bromide) test

L929 fibroblast cells (Royan Institute, Yazd, Iran) were cultured in complete Dulbecco's Modified Eagle Medium (DMEM) supplemented with 100 U/mL penicillin and 100 µg/mL streptomycin (Hyclone, USA). Cells were seeded into 24-well plates at a density of 10,000 cells/well and maintained under a humidified atmosphere of 95% air and 5% CO_2 at 37 °C (Memert Jppssplus). After 24 h, cells were treated with nanocomposite suspensions at a final concentration of 5 mg/mL of nano composite. Treated and control cells were incubated for 24 h and 7 days under the same conditions. Following incubation, MTT solution was added to each well and incubated for 4 h at 37 °C. The medium was then carefully removed, and formazan crystals were dissolved in solubilizing buffer. Samples were further incubated for 1 h to ensure complete dissolution. The resulting purple solution was quantified by measuring absorbance at 570 nm using an ELISA reader (Convergent EL-Reader 96X, Germany) (Manafi et al., 2019b; Manafi et al., 2019a; Rahaman and Mao, 2005). Cell viability was calculated relative to control wells (untreated cells), allowing assessment of the cytotoxic effect of nanocomposite exposure. This protocol ensures reproducible measurement of metabolic activity while accounting for potential variations in nanoparticle dissolution and ion release.
The following formula is then applied to determine the survival rate:

$$\text{Cell Viability}\% = \frac{ODs}{ODc} \tag{2}$$

ODs Optical Density Sample, *ODc* Optical Density Control (Manafi et al., 2019b; Manafi et al., 2019a). The steps are represented in Fig. 2.

2.2.7 The antibacterial assay

The antibacterial activity of the nanocomposites was assessed against Streptococcus mutans (IBRC-M 10682). Samples (discs, 10 mm $\times$ 1 mm) were sterilized and incubated with bacterial suspensions in BHI medium at 37 °C, 160 rpm. After exposure, aliquots were serially diluted ($10^{-1} - 10^{-6}$) in physiological saline (0.4% NaCl, pH 7.4), plated on BHI agar, and incubated for 24 h. Colony-forming units (CFU) were counted (Sana SL-902), and antibacterial efficiency was expressed as percentage reduction relative to the control using Eq. (3)

$$R = \frac{B - A}{B} \times 100 \tag{3}$$

where, R indicates the inhibition efficiency, B is the number of colonies in the control group, and A is the number of colonies resulting from inhibition of the material at different inhibition (Seyedmajidi et al., 2018).

3. Results and discussion

3.1 Phase analysis of nano composites

The XRD patterns of the FA–BG nanocomposites containing 10, 20, and 30 wt.% S53P4 were shown in Fig. 3, which exhibited reflections characteristic of the fluoroapatite ma-

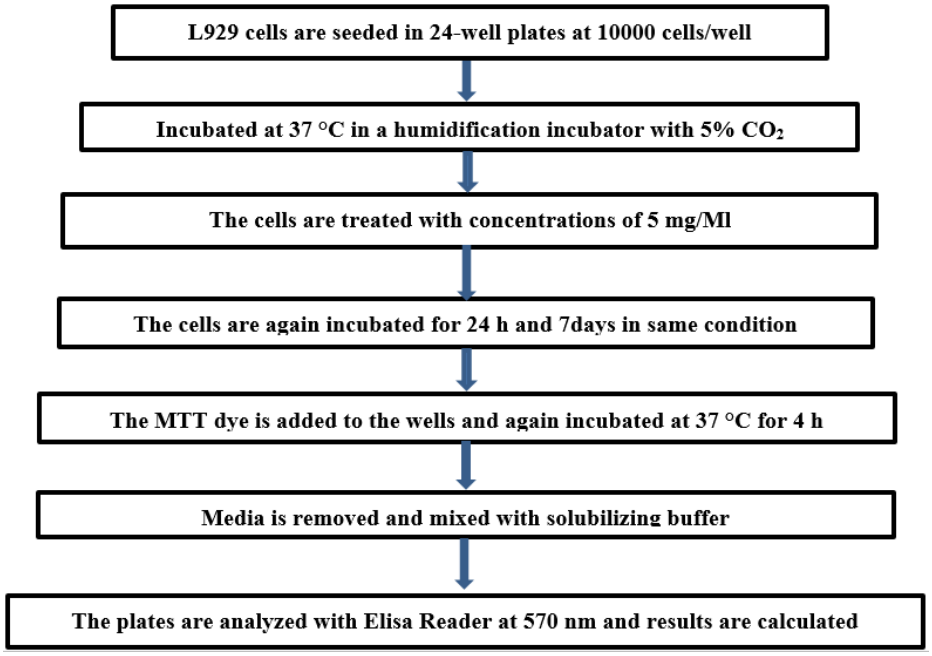

Figure 2. Flowchart of MTT assay.

trix, confirming that the crystalline FA phase was preserved. The amorphous phase of the S53P4 glass overlaped with the FA peaks in the rang of $2\theta = 25 - 35°$, resulting in slight peak broadening and minor shifted due to the influence of the amorphous background. Based on the Landi equation, the crystallinity of the nanocomposites decreased with increasing glass content, estimated at $\sim$ 86%, 71%, and 67% for 10, 20, and 30 wt.% S53P4, respectively. Scherrer analysis further indicated a reduction in FA crystallite size from $\sim$ 28 nm to 24 nm and 20 nm with increasing BG content, reflecting the effect of the amorphous glass phase on crystal growth.

3.2 Morphological investigation of nanocomposites

In this report, the S53P4 bioglass was successfully incorporated into the matrix of fluorapatite and yielded FA-BG nanocomposites. Field emission scanning electron microscopic (FESEM) images of FA-BG nanocomposites with different S53P4 bioglass percentages were revealed in Fig. 4 (a-c). As it was seen in Fig. 3, the FA-BG nanocomposites demonstrated a good dispersion with a regular shape. The figure clearly shows the uniform distribution of the S53P4 bioglass phase.

The EDS spot analysis and map of the FA–BG nanocomposites containing 10, 20, and 30 wt.% S53P4 were shown in

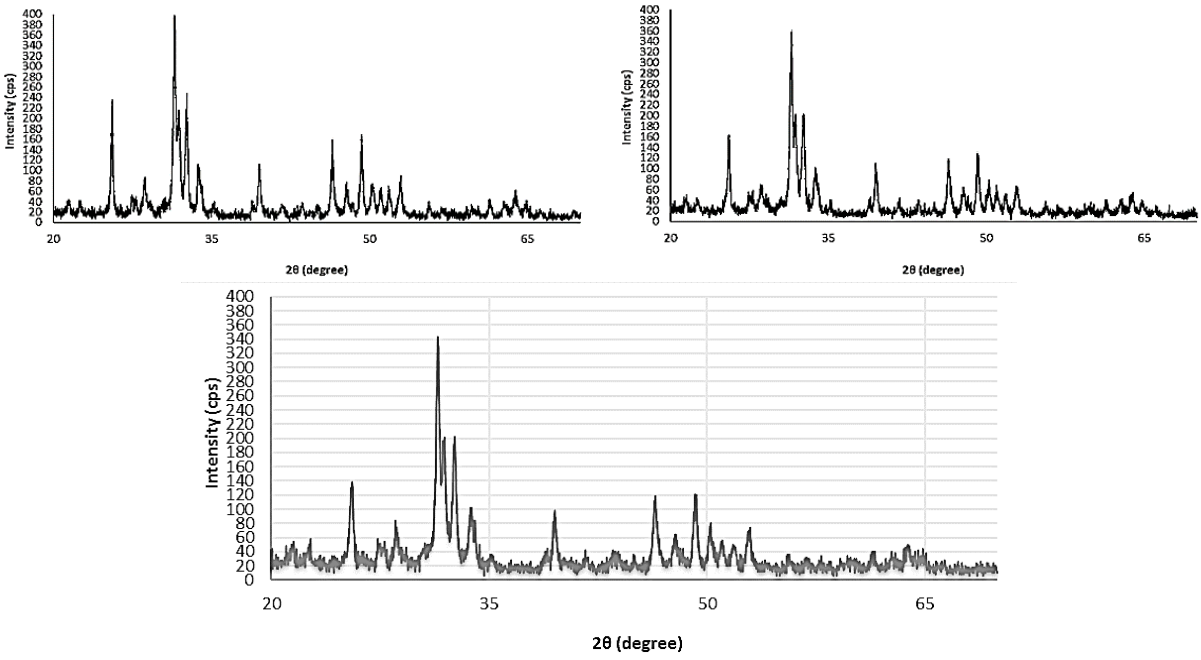

Figure 3. X-ray diffraction patterns of FA-BG nanocomposites (a) FA-BG-10, (b) FA-BG-20, (c) FA-BG-30.

Fig. 5(a-e) which revealed prominent peaks corresponding to oxygen, fluorine, silicon, phosphorus, and calcium, with no detectable signals from extraneous elements. This observation confirms the high elemental purity of the synthesized nanocomposites and indicates the successful incorporation of the bioactive glass and fluoroapatite phases without contamination.

3.3 Investigation of degradation and biocompatibility

To study biocompatibility and biodegradability of analyses on samples, after SBF immersion and ion concentration from the SBF solution, some tests were performed as follows:

As it is shown in the diagram in Fig. 6(a), the samples underwent fast weight loss on the first day and reduced until 7 days, then have remained reasonably stable since the 21 days. On the first day, the samples were washed by im-

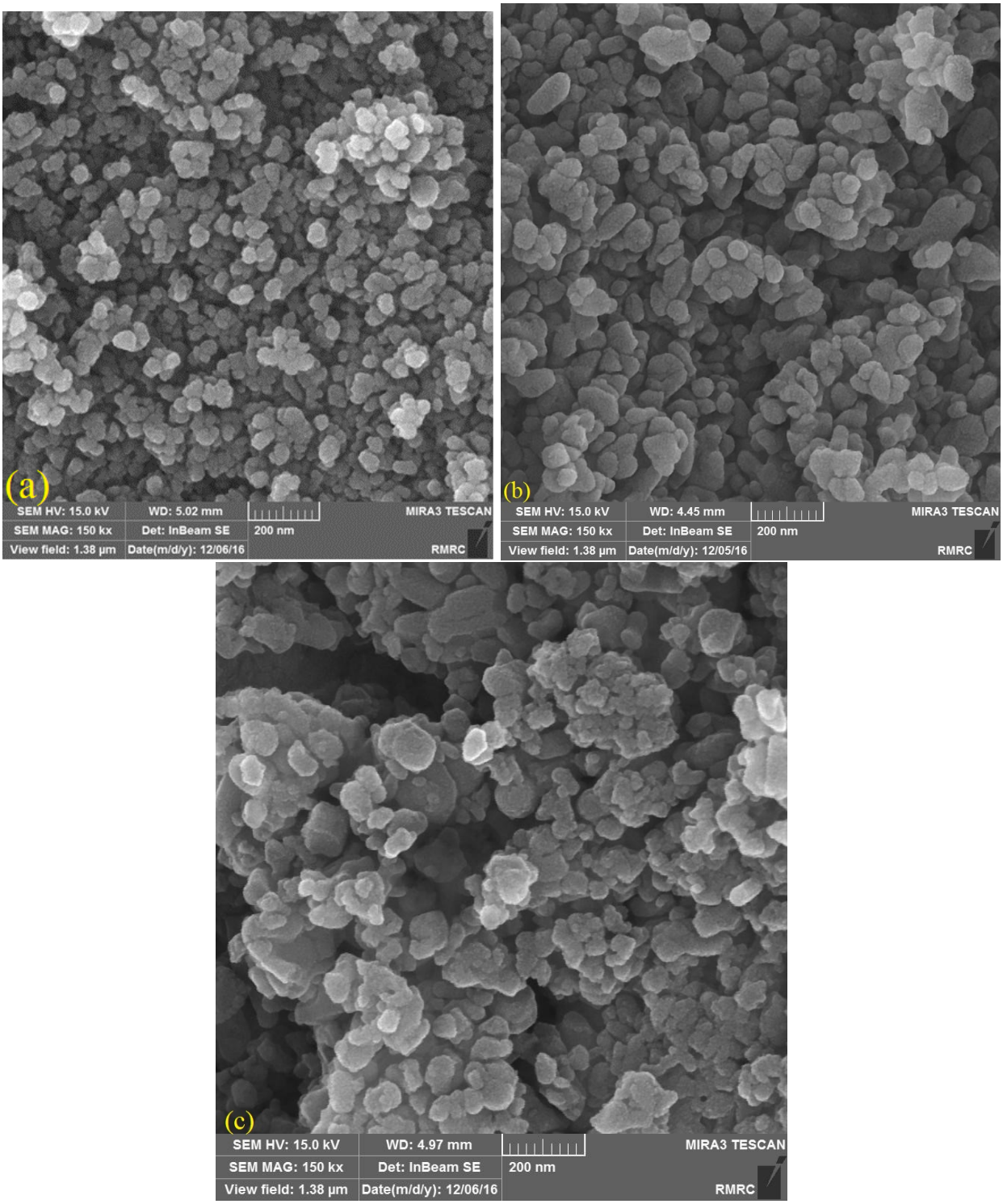

Figure 4. Field emission scanning images of FA-BG nanocomposites (a) FA-BG-10, (b) FA-BG-20, (c) FA-BG-30.

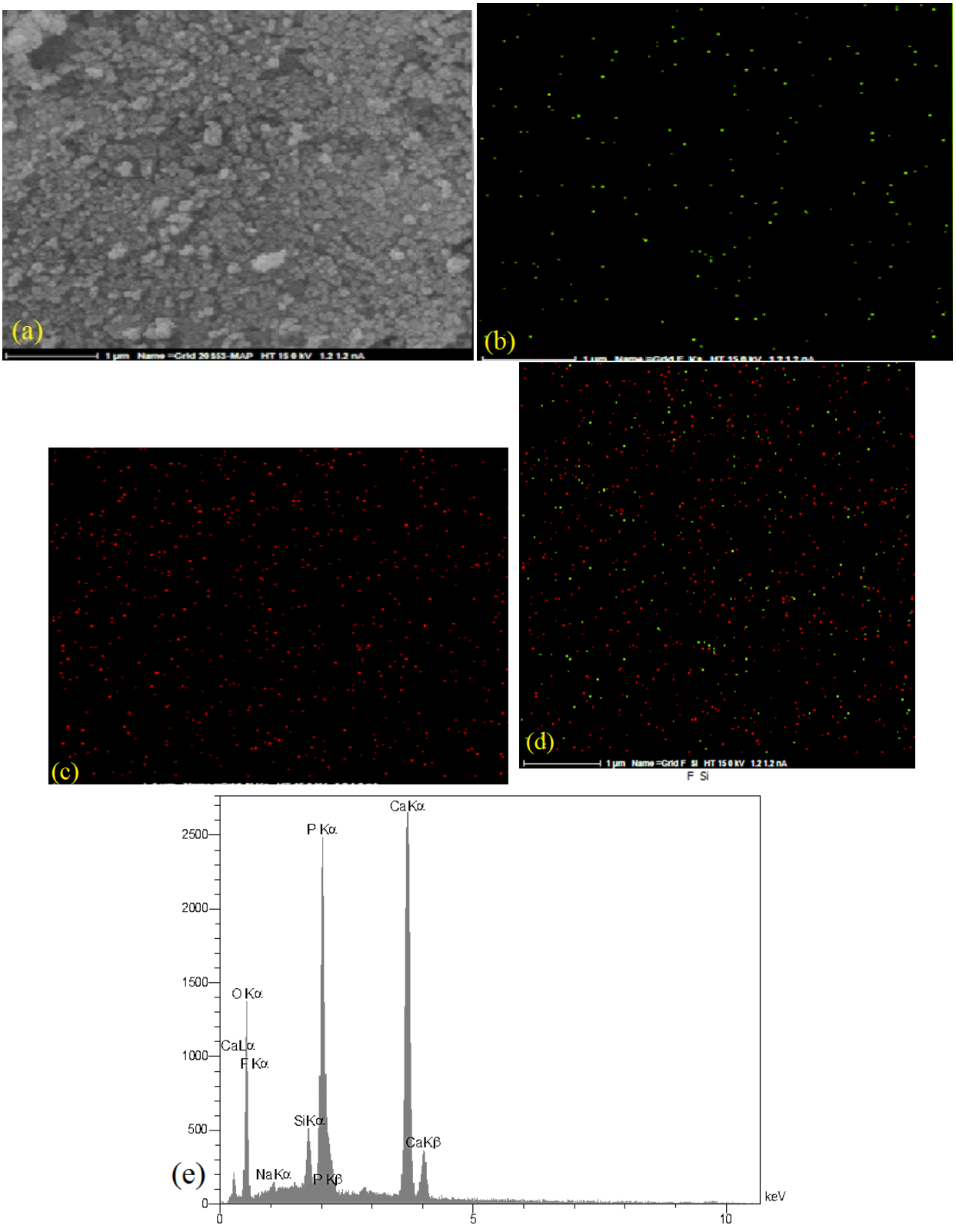

Figure 5. (a) Image obtained from nanocomposite of structural pattern Map-EDS of FA-BG nanocomposites, (b) Fluorine in FA-BG nanocomposite from EDS pattern, (c) Silicon in FA-BG nanocomposite from EDS pattern, (d) F and Si in FA-BG nanocomposite from EDS pattern, (e) Elements in FA-BG nanocomposite from EDS pattern.

mersion in the solution. After immersion of the samples in the SBF solution, the weight change of the samples was considered. The following diagram shows the rapid weight loss of samples the first day of 21 days of immersion in SBF solution. However, a constant rate of weight loss could be seen from 7 to 21 days. By immersion in the solution, the apatite layer formed on the surface of samples. By time increase, the thickness of the layer increased, while the rate of the loss of weight decreased. The stability of the calcium phosphate phases expressively depended on the tempera-

ture. Each calcium phosphate phase was able to convert to hydroxyapatite in the existence of adequate water which could be attributed to the existence of calcium phosphate compounds in the synthesized composite sample. When this sample was located nearby to the body fluid simulator, this hydroxyapatite layer initiated to form. The initiation in the solution raised and the pH changed fast with the creation of the apatite layer (Pandayil et al., 2024; Välimäki and Aro, 2006). Moreover, with the amount of bioactive S53P4 glass phase in the composite sample, the amount of degradation and weight loss increased, which could be endorsed to the higher solubility of bioactive S53P4 glass phase incompatible with the fluorapatite (Jones, 2013; Bigoni et al., 2019). The reason for this weight loss trend can be attributed to the gradual formation of the bioactive apatite layer on the surface of the samples. Gradually, as the samples remain in the SBF solution for an extended period of time, the apatite layer is also gradually formed and its thickness increases. This prevents further leaching/dissolution of the samples, so that with increasing layer thickness, the leaching rate becomes more constant and less fluctuating, and subsequently the weight loss rate becomes more balanced. Due to the amorphous structure of the bioactive S53P4 glass phase and consequently its greater solubility, increasing the weight percentage of this additive in the fluoroapatite-based nanocomposite will lead to increased leaching and weight loss, as the results also confirm this.

The diagram of pH changes in terms of immersion in the SBF solution is shown in Fig. 6(b),which completed some observations concerning the weight loss. During the initial hours and first day, the pH of the SBF solution undergoes a significant increase, which can be attributed to the explosive release of ions such as calcium, silicon, and phosphate (from glass) and calcium, phosphate, and fluorine (from fluoroapatite) were substituted in the environment. Thus, on the first day and directly after immersion of the samples in the simulator solution, the release of the elements of the samples was greater which produced a great change and caused the pH of the SBF solution to improve melodramatically. By creating a bioactive layer on the samples, this release was stabilized and banned a quick change in the pH of the solution and finally reaches a relatively constant leve. The apatite layer formed on the surface of the nanorod creates a kind of barrier resistant to leaching/ion release and prevents the increase in the pH of the solution caused by the release of ions (especially alkaline ions such as calcium). As the composites remain in solution for longer and the apatite layer on their surface becomes thicker, more resistance is provided to ion release until the solution pH reaches a relatively constant fluctuation rate (Välimäki and Aro, 2006; Jones, 2013; Manafi et al., 2019b). Obviously, as the immersion of composite increased and the thicker apatite layer on their surface become more impermeable to ion release, there was a gradual decrease in the pH until it remains relatively constant. Nanocomposites containing higher amounts of S53P4 bioglass underwent more severe changes in pH, which might be due to their higher permeability of silicon and magnesium ions (Hoppe et al., 2011). The FA sample increased the pH, which might have recommenced the formation of the hydroxyapatite layer by release of the ion (Pandayil et al., 2024). It can be observed from the chart that,on the first day, the sample is a biological environment with almost the most changes. Additionally, from the review of the pH graph and the weight change chart, it could be determined that the sample containing 30% of BG nanoparticles experienced the creation of the apatite layer more than other samples. For the sample of FA-BG-30 after 7 days, the pH has improved, which could be endorsed to the beginning of the destruction of the sample in the SBF. As previously mentioned, nanocomposites containing higher amounts of bioactive glass nanoparticles cause more severe fluctuations in solution pH due to their higher ion release potential. The release profiles of fluoride and silicon ions are presented in Fig. 6(c) and (d). Upon immersion of the synthesized composites in simulated body fluid (SBF), ion exchange with the surrounding medium was initiated, resulting in measurable changes in ion concentrations. As fluoride and silicon were absent in the initial SBF composition, their concentration changes provided a suitable indicator of composite biodegradability. The composites demonstrated enhanced bioactivity in the simulated physiological environment, attributed primarily to the release of Si^{4+} ions. The formation and growth of an apatite layer on the composite surface were directly influenced by the ion release rate of the original materials (Manafi et al., 2019b; Ylänen, 2017). The fluoride release behavior of fluorapatite was comparable to the silicon release from bioactive glass, exhibiting the highest ion release within the first 24 hours, followed by a gradual decrease. This reduction is likely due to the formation of a bioactive apatite barrier, which slows further ion diffusion and leads to a relatively stable release profile (Hoppe et al., 2011). Analysis of ion release patterns from fluorapatite nanoparticles, S53P4 bioactive glass, and fluorapatite–S53P4 nanocomposites containing 10, 20, and 30 wt.% S53P4 reveals two key observations: (i) all samples displayed a similar release trend, with maximum ion release occurring during the initial stage (primarily within the first seven days), followed by a gradual decline as the apatite barrier formed, eventually reaching a steady-state; and (ii) increasing the proportion of bioactive glass or decreasing the fluorapatite content resulted in higher overall ion release.The process of cumulative release of ions at different times indicates that the release of ions would follow the first-order kinetics with the following general relation:

$$\ln C = -mt + \ln C_0 \tag{4}$$

where C was the ion concentration at the time of t, C_0 constant (initial concentration), and m which could be realized from the slope of the $\ln C$ line at the time of t, the ion release rate constant was an appropriate criterion for judging the rate of ion release from nanocomposites Accordingly, the calculated values of m are presented in the following Table 2 and logarithmic results of silica release are existed in the Table 3.

Regarding the kinetic data, the constant ion release rate did not have a direct relationship with the amount of ion storage in the source material. As it was observed, the release rate constants of fluoride and silicon ions were the highest in the

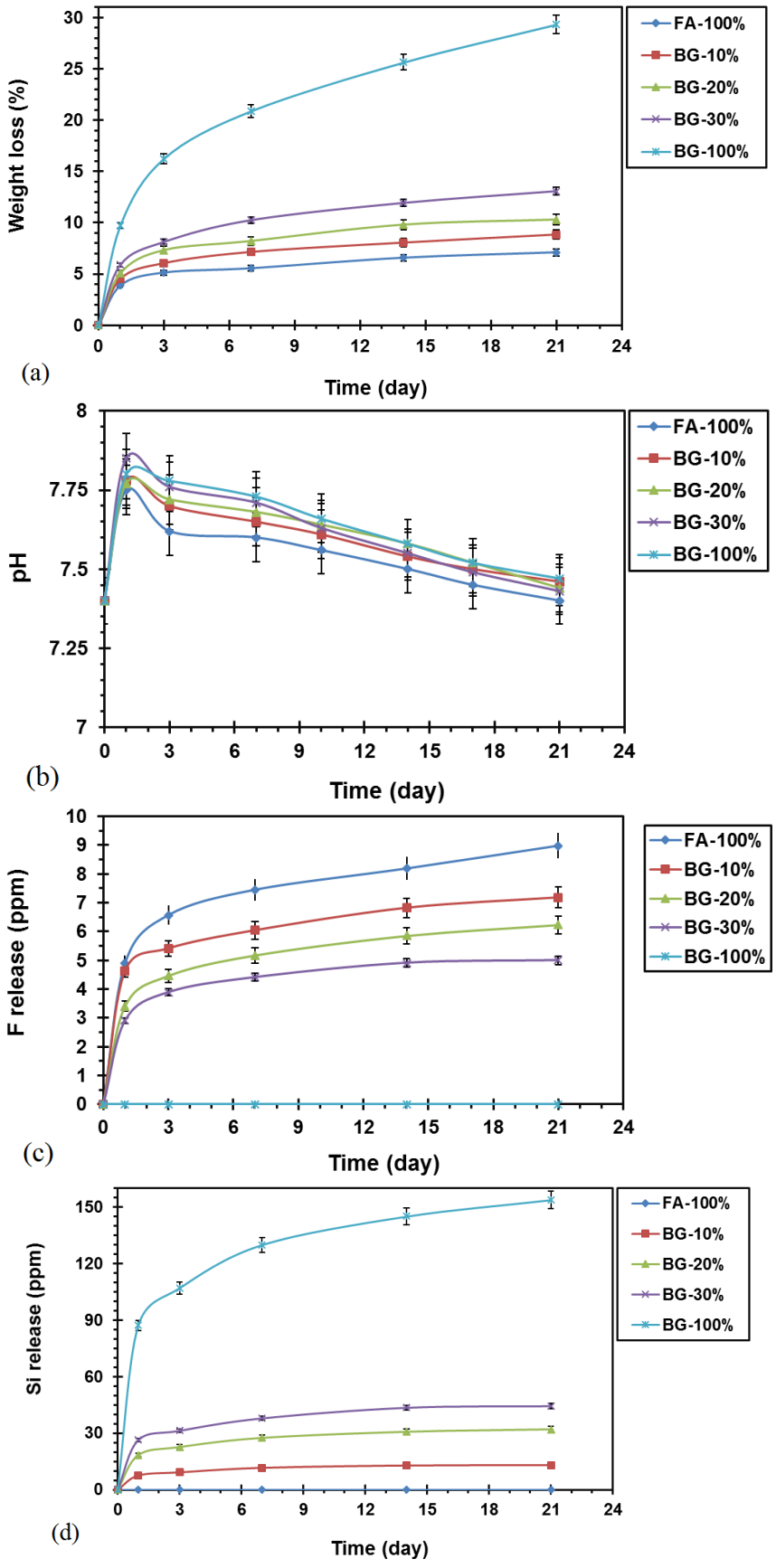

Figure 6. Weight change percentage of nanocomposites in SBF, (a) Graph of pH changes of nanocomposites in SBF, (b) Release graph of fluorine ion in SBF, (c) Release graph of Si ion in SBF solution (d).

FA-BG-30 .The durability of fluoride and silicon ion release for FA-BG-30 nanocomposites was the highest compared to other samples. Based on the kinetic data as well as recent results on bioactivity and degradability, the FA-BG-30 nanocomposite was the best option for future biomedical research.

Ion release profiles of the nanocomposit also was characterized based on the Korsmeyer–Peppas empirical model.

$$\frac{M_t}{M_\infty} = kt^n \tag{5}$$

where:

- M_t: The amount of drug released at time t.
- M_∞: The total amount of drug available for release (equilibrium).
- k: The release rate constant, incorporating structural and geometric characteristics of the system.
- n: The release exponent (diffusional exponent), which indicates the predominant release mechanism (42).
- $n \approx 0.5$, Fickian diffusion, where the release is primarily controlled by drug diffusion through the matrix.
- $n \approx 1$ Case-II transport, where the release is controlled mainly by polymer relaxation, swelling, or erosion processes.
- $n < 1$: Anomalous (non-Fickian) transport, where drug release is governed by a combination of diffusion and matrix swelling/erosion (Hoppe et al., 2011).

Calculated values of n and k are presented in Table 4. Based on the obtained values for n, it can be claimed that according to the Korsmeier-Peppas model, the ion release mechanism (both fluoride anion and silicon cation) in fluoroapatite nanoparticles and S53P4 bioactive glass as well as fluoroapatite-S53P4 bioactive glass nanocomposites consisting of 10, 20 and 30 wt.% of S53P4 bioactive glass is of diffusion type and follows Fick's diffusion law.

Based on the kinetic calculations performed, several points are worth mentioning:

- The ion release rate constant is directly related to the ion storage rate in the source material, so that the highest fluoride and silicon ion release rate constants were obtained for FA-100% and BG-100% nanoparticles, respectively.
- The reduction in the release rate of each ion in the composite sample is solely due to the reduction of the ion source, and it does not seem that the second component of the composite has an adverse effect on the release of the counterion;
- It seems that a nanocomposite such as BG-20% is an interesting option for future biomedical research due to its desirable release capability of each of the silicon and fluoride ions, as well as its suitable bioactivity and biodegradability.

Table 2. Logarithmic results of fluoride release in 10, 20, and 30% bioglass (SBF).

log (t/hour)	Log C				
Day	Results of fluoride release				
	FA-100%	BG-10%	BG-20%	BG-30%	BG-100%
1.3802112	0.69108149	0.666518	0.5327544	0.463893	0
1.8573325	0.81756537	0.7331973	0.6493349	0.5899496	0
2.22553093	0.87215627	0.7810369	0.7134905	0.6444386	0
2.5263393	0.9132839	0.8337844	0.7671559	0.6910815	0
2.7024305	0.95327634	0.8561244	0.794488	0.69897	0

Table 3. Logarithmic results of silica release in 10, 20 and 30% bioglass (SBF).

log (t/hour)	Log C				
Day	Results of Si release				
	FA-100%	BG-10%	BG-20%	BG-30%	BG-100%
1.380211242	0	0.8785218	1.2655253	1.4207806	1.940068
1.857332496	0	0.9652017	1.3558345	1.4962375	2.029384
2.2255309282	0	1.0629578	1.4396484	1.5790973	2.113676
2.526339277	0	1.1065309	1.4877039	1.6390879	2.161458
2.702430536	0	1.1142773	1.5054213	1.6474808	2.186815

Table 4. Calculated values of *n* and *k* release rate constant for fluoroapatite-S53P4 bioactive glass nanocomposites.

Sample	Release of Si^{4+}		Release of F^{-}	
	N	K	N	K
BG-100%	47.785	0.190	0	0
BG-10%	4.190	0.189	2.921	0.144
BG-20%	12.621	0.187	1.872	0.196
BG-30%	14.733	0.182	1.727	0.178
FA-100%	0	0	2.779	0.190

3.4 Bioactivity of nano composites

SEM–EDX analyses of FA, S53P4 bioactive glass, and FA–S53P4 nanocomposites (10, 20, and 30 wt.% BG) after 1 and 21 days of SBF immersion (Fig. 7) revealed the formation of a uniform nanocrystalline apatite layer across all samples, confirming their intrinsic bioactivity according to the Kokubo–Takadama criterion (Kokubo and Takadama, 2006). The coexistence of FA as a phosphate-rich, structurally stable phase and S53P4 as an ion-releasing, highly reactive phase generated a supersaturated interfacial environment conducive to rapid apatite nucleation. Increasing BG content from 10 to 30 wt.% did not significantly alter apatite morphology, suggesting that once a critical reactivity threshold is achieved, further BG addition becomes limited by ionic diffusion rather than surface chemistry (Pandayil et al., 2024; Rezwan et al., 2006; Kokubo and Takadama, 2006). The observed petal-like and cabbage-like nanocrystals, typical of *in vitro* apatite growth, are known to enhance protein

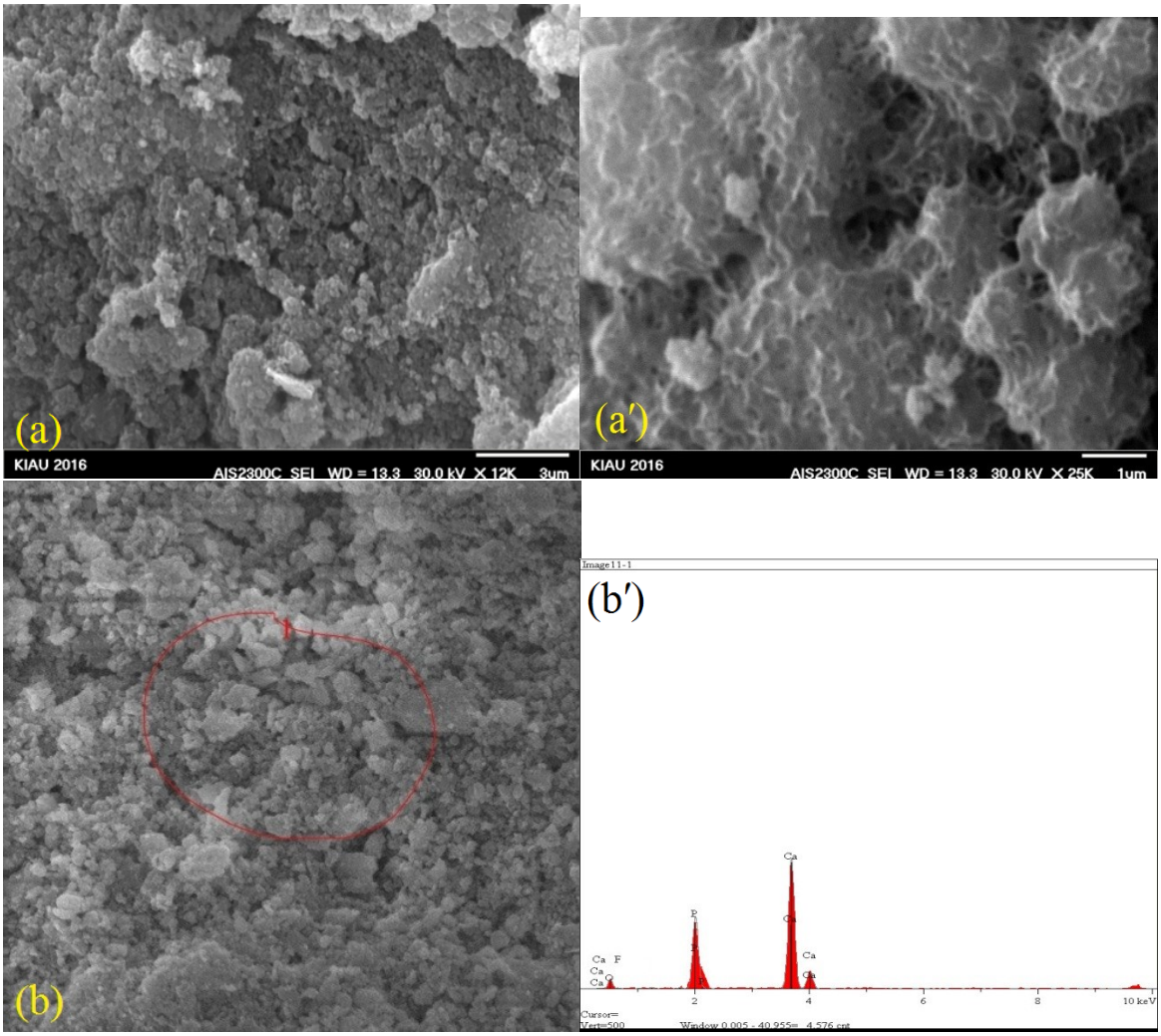

SEM image of (a): FA powder after 1 day of immersion, (a′,b): FA powder after 21 days of immersion with two magnification, (b′): EDX image of the FA, (c): FA-BG-10 after 1 day of immersion (c′,d): FA-BG-10 after 21 day of immersion with two magnification, (d′): EDX image of the FA-BG-10, (e): FA-BG-20 after 1 day of immersion, (e′,f) FA-BG-20 after 21 day of immersion with two magnification (f′): EDX image of the FA-BG-20, (g): FA-BG-30 after 1 day of immersion (g′,h): FA-BG-30 after 21 days of immersion with two magnification, (h′): EDX image of the FA-BG-30

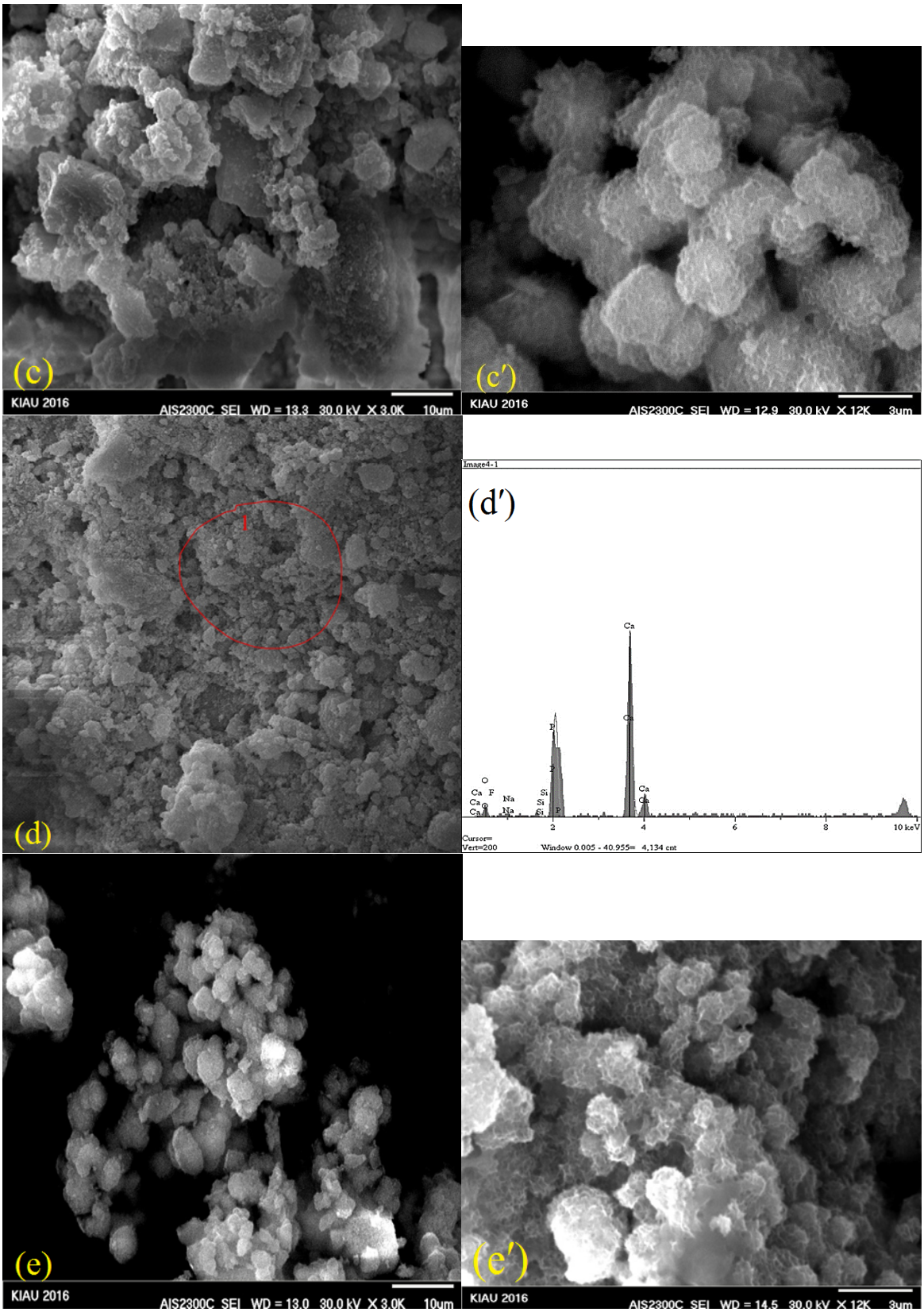

SEM image of (a): FA powder after 1 day of immersion, (a′,b): FA powder after 21 days of immersion with two magnification, (b′): EDX image of the FA, (c): FA-BG-10 after 1 day of immersion (c′,d): FA-BG-10 after 21 day of immersion with two magnification, (d′): EDX image of the FA-BG-10, (e): FA-BG-20 after 1 day of immersion, (e′,f) FA-BG-20 after 21 day of immersion with two magnification (f′): EDX image of the FA-BG-20, (g): FA-BG-30 after 1 day of immersion (g′,h): FA-BG-30 after 21 days of immersion with two magnification, (h′): EDX image of the FA-BG-30

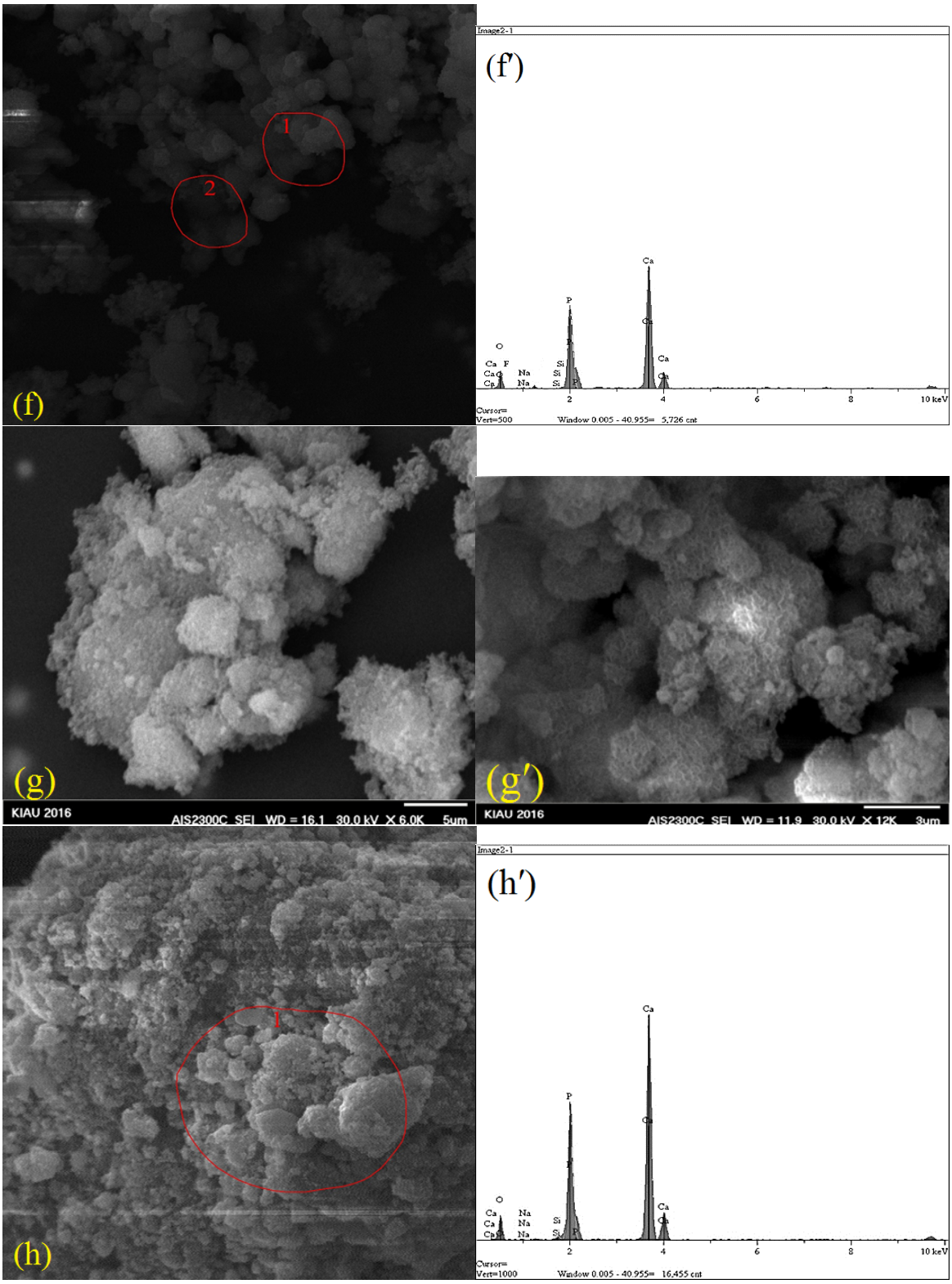

Figure 7. SEM image of (a): FA powder after 1 day of immersion, (a′,b): FA powder after 21 days of immersion with two magnification, (b′): EDX image of the FA, (c): FA-BG-10 after 1 day of immersion (c′,d): FA-BG-10 after 21 day of immersion with two magnification, (d′): EDX image of the FA-BG-10, (e): FA-BG-20 after 1 day of immersion, (e′,f) FA-BG-20 after 21 day of immersion with two magnification (f′): EDX image of the FA-BG-20, (g): FA-BG-30 after 1 day of immersion (g′,h): FA-BG-30 after 21 days of immersion with two magnification, (h′): EDX image of the FA-BG-30.

adsorption and osteoblast attachment (Hoppe et al., 2011; Gatti et al., 2024; Rahaman and Mao, 2005). EDX results supported these observations: Ca intensities consistently exceeded P, and FA-rich samples exhibited Ca/P atomic ratios approaching the stoichiometric hydroxyapatite value (~ 1.67). Composites containing higher S53P4 fractions showed slightly lower Ca/P ratios due to the glassy phase contribution. Although semi-quantitative, these trends provide indirect confirmation of progressive apatite deposition during SBF immersion (Välimäki and Aro, 2006; Kokubo and Takadama, 2006; Vallet-Regí et al., 2022; Gerhardt and Boccaccini, 2010a).

The underlying mechanism aligns with Hench's five-stage model (1998): Initial Ca^{2+}/H^{+} exchange, formation of silanols, dissolution into $Si(OH)_4$, formation of a SiO_2-rich layer, and subsequent precipitation/crystallization of a $CaO–P_2O_5$ phase into carbonate-substituted apatite (Hench and Wilson, 2013; Jones, 2013). Incorporation of F^{-} into the apatite structure induced slight lattice contraction, reflected by the ~ 5 cm^{-1} shift in the $\nu_1 (PO_4^{3-})$ Raman band (~ 960 cm^{-1}), consistent with earlier reports (**a53**; Zhao, 2008; Feroz and Khan, 2020). This fluorine-induced structural tightening reduces solubility and promotes surface stability-features linked to improved long-term osteointegration (Kazimierczak et al., 2023). Overall, FA–S53P4 nanocomposites benefit from synergistic interactions: FA offers crystallographic stability and nucleation templates, while S53P4 enhances ionic reactivity and accelerates mineralization. This balanced dual functionality produces rapid yet controlled bioactivity and structurally refined apatite phases, making the composites strong candidates for bone-tissue-engineering applications requiring both reactivity and durability.

3.5 Raman spectroscopy analysis

The Raman spectra of fluoroapatite (FA), S53P4 bioactive glass, and FA–S53P4 nanocomposites (10, 20, and 30 wt.% BG) after 21 days of immersion in SBF in Fig. 8 (a-c) exhibited a consistent and characteristic feature across all samples: the emergence of an intense band at ~ 960 cm^{-1}, corresponding to the symmetric stretching vibration (ν_1) of the PO_4^{3-} group. This peak is widely recognized as the fingerprint of hydroxyapatite, and its dominance indicates the formation of a continuous nanostructured apatite layer that effectively masks the underlying signatures of the starting materials (FA or S53P4). The suppression of the parent-phase peaks is attributed to the limited penetration depth of Raman spectroscopy and the substantial thickness of the newly formed apatite layer, consistent with previous observations (Amaury et al., 2022; Madupalli et al., 2017). In addition to the phosphate band, a secondary peak emerged at ~ 1080 cm^{-1} in all samples following immersion. This feature is assigned to the stretching mode of CO_3^{2-} groups in a B-type substitution within the apatite lattice or, in some cases, to calcite-related carbonate vibrations. The presence of this band provides strong evidence of carbonate incorporation into the apatite structure, giving rise to the formation of biologically relevant carbonate apatite, which more closely mimics the mineral phase of natural bone (Fleet, 2009; Zhou and Lee, 2011). Such carbonate substitution is known to enhance the dissolution rate, bioactivity, and cellular response of apatite coatings, thereby reinforcing the osteoconductive potential of the composites (Madupalli et al., 2017). The consistent observation of these Raman

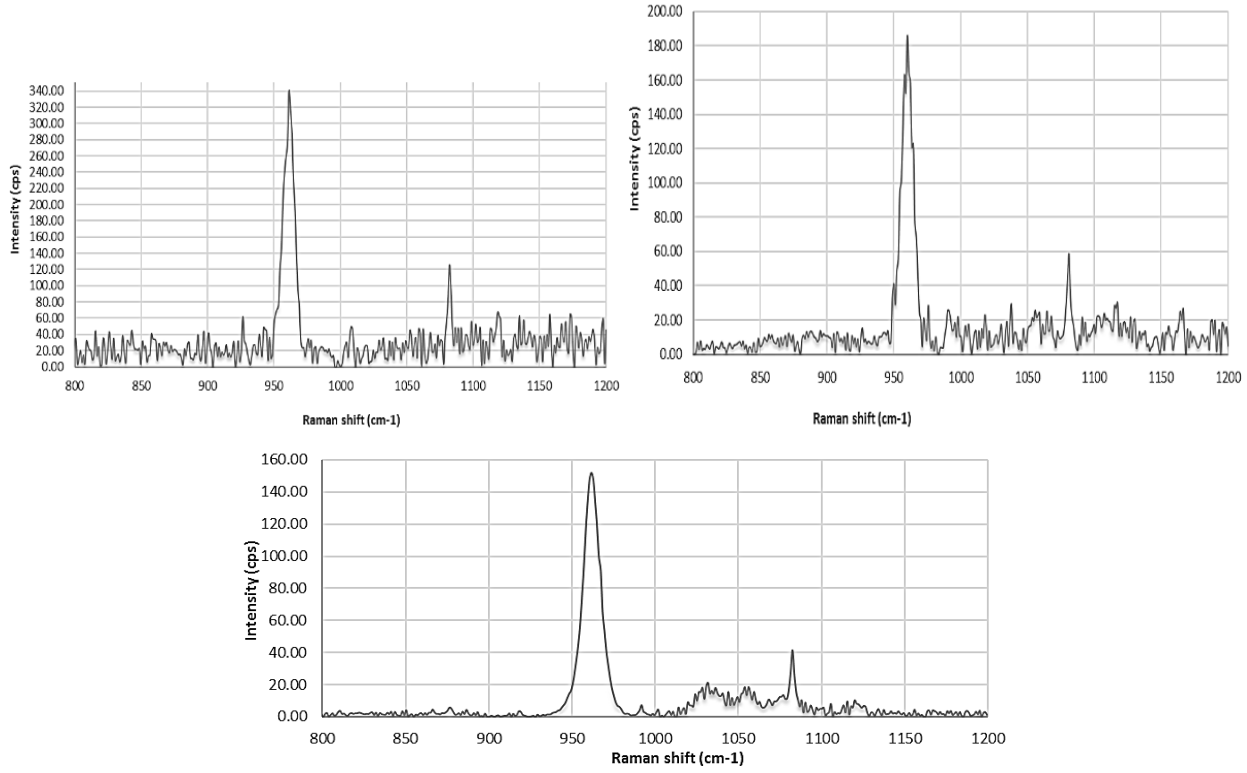

Figure 8. Spectroscopic test of FA-BG nanocomposites (a) FA-BG-10, (b) FA-BG-20, (c) FA-BG-30 after 21 days in solution.

signatures, regardless of the proportion of S53P4 bioactive glass, demonstrates that the composites share a common bioactive mechanism: Rapid nucleation and maturation of a carbonate-substituted hydroxyapatite layer in SBF. This finding aligns with the classical definition of bioactivity proposed by Kokubo and Takadama (Kokubo and Takadama, 2006), while also highlighting the synergistic contribution of FA (providing crystallographic templates for apatite nucleation) and S53P4 (supplying Ca^{2+} and PO_4^{3-} ions through dissolution). Ultimately, the Raman evidence strongly supports the capacity of FA–S53P4 composites to replicate the mineral chemistry of bone, confirming their suitability for applications in bone tissue engineering.

3.6 Cell viability (MTT Assay)

MTT assay results after 7 days of incubation (Table 5) showed a general increase in cell viability for all groups, including the experimental FA–S53P4 composites and control samples. Among the tested formulations, the composites containing 10 and 20 wt.% bioactive glass demonstrated a more favorable cellular response compared with pure FA and the 30 wt.% BG sample. The FA–BG–20 formulation exhibited the highest metabolic activity, exceeding both FA–BG–10 and FA–BG–30.This trend reflects the critical influence of ion-release kinetics on cytocompatibility. At 10 wt.% BG, the released concentrations of Ca^{2+}, Si^{+4}, and PO_4^{3-} may be too low to strongly stimulate metabolic pathways, whereas at 30 wt.% BG, rapid dissolution can result in excessive Na^+ and Ca^{2+} accumulation, increased osmolarity, and localized pH elevation-conditions known to suppress cell adhesion and viability. The 20 wt.% composition provides a more balanced ionic environment, supporting optimal metabolic activity. These observations are consistent with reports showing that moderate levels of bioactive glass enhance osteoblast proliferation, while overly aggressive ion release can lead to cytotoxic effects (Xynos et al., 2001; Kaur et al., 2019; Gerhardt and Boccaccini, 2010b). Thus, FA–BG–20 represents a compositionally optimized system in which bioactivity and cytocompatibility are effectively balanced (Hench and Wilson, 2013; Rahaman et al., 2011). Although the maximum viability observed in the present study was approximately 60%, this value does not necessarily indicate poor cytocompatibility. Several factors intrinsic to extract-based MTT assays such as the use of undiluted extracts, ion-rich media, and exposure 7-day static without medium renewal can reduce metabolic activity relative to untreated controls, even for materials known to be clinically safe. Furthermore, bioactive glasses commonly induce transient pH shifts during early ion exchange, which can temporarily suppress metabolic activity without causing permanent cytotoxicity. Similar viability ranges (50–70%) have been reported for S53P4-based materials and other ion-releasing bioceramics during early exposure, despite their established safety *in vivo*. Overall, the viability profile—especially the superior response of FA–BG–20—supports the conclusion that the synthesized nanocomposites are cytocompatible and that their biological performance is strongly dependent on the fine balance between FA stability and BG-driven ionic reactivity (Xynos et al., 2000).

3.7 Antibacterial activity of FA–S53P4 nanocomposites

The antibacterial performance of FA–S53P4 nanocomposites was quantitatively assessed via colony-forming units (CFU) after 24 h incubation. As shown in Table 6 and Fig. 9 (a-c), increasing the S53P4 content significantly enhanced bacterial inhibition. Specifically, pure S53P4 exhibited the highest antibacterial effect, achieving approximately 90% reduction in CFU relative to the negative control, while pure FA showed a modest $\sim$ 25% inhibition. Among the

Table 5. MTT cell survival test for all samples after 7 days.

Sample	Cell viability	Standard deviation
FA 100%	0.382	0.031
S53 100%	0.2160	0.029
S53 30%	0.292	0.024
S53 20%	0.593	0.041
S53 10%	0.479	0.031
Control	0.59	0.02223

Table 6. The antibacterial performance of FA–S53P4 nanocomposites.

Sample	S53P4 content (wt.%)	CFU reduction (%)	Notes on cytocompatibility
FA	0	25	High cell viability
FA–BG–10	10	55	Good viability
FA–BG–20	20	75	Optimal balance
FA–BG–30	30	85	Slight reduction in viability
S53P4	100	90	Reduced viability

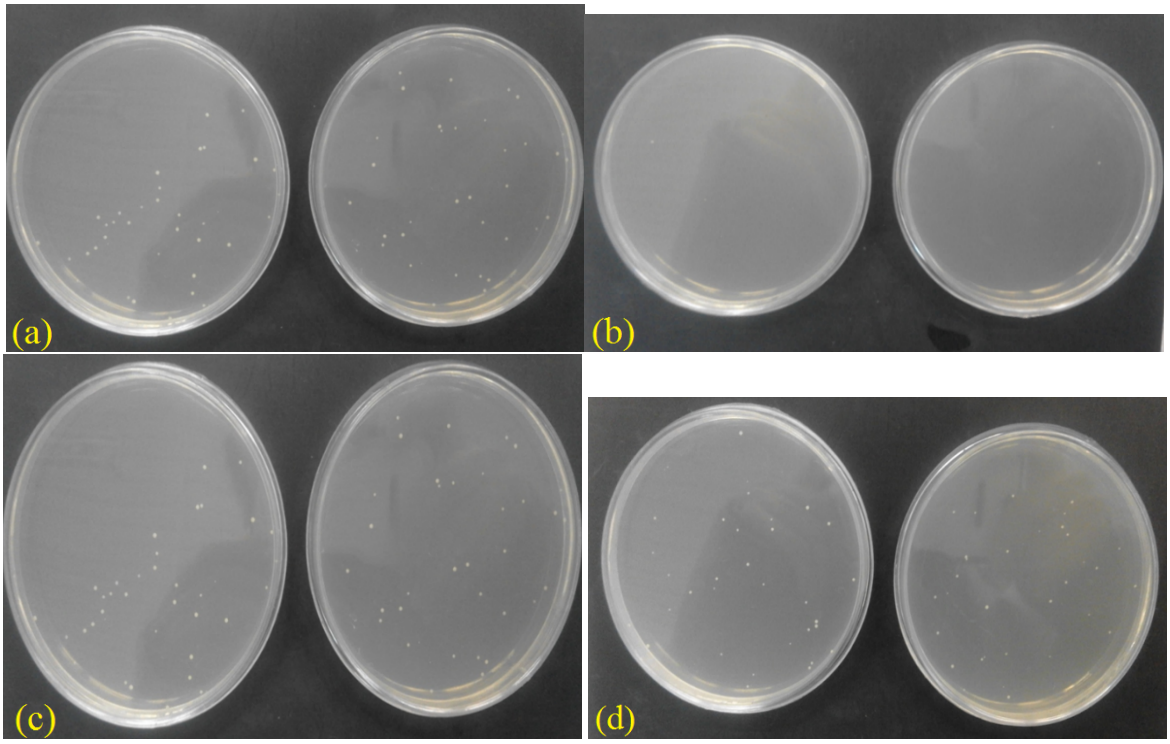

Figure 9. Image of the bacterial activity of (a) 100% fluoroapatite, (b) Image of the bacterial activity of 100% BG activity of 10 BG, (c) Image of the bacterial activity of 20% BG, (d) Image of the bacterial activity of 30% BG, (e) Image of the bacterial activity of 30% BG.

composites, FA–BG–10 and FA–BG–20 demonstrated intermediate effects ($\sim$ 55% and $\sim$ 75% CFU reduction, respectively), whereas FA–BG–30 approached the antibacterial activity of pure BG but displayed slightly reduced cell viability Mechanistically, the enhanced antibacterial activity correlates with the ionic dissolution of S53P4 (Na^{+}, Ca^{2+}, PO_4^{3-}) and the subsequent increase in local pH and osmotic pressure, creating conditions unfavorable for bacterial proliferation (Hench and Wilson, 2013; Jones, 2013; Rahaman and Mao, 2005; Gerhardt and Boccaccini, 2010b; Rahaman et al., 2011). Fluoroapatite contributes additional mild antibacterial action through fluoride release, without significantly affecting mammalian cell viability. These results indicate that moderate BG loading ($\sim$ 20 wt.%) provides an optimal balance between antibacterial efficacy and cytocompatibility, making FA–BG–20 a promising candidate for bone tissue engineering applications requiring infection prevention.

4. Conclusion

Fluorapatite–S53P4 bioactive glass (FA–BG) nanocomposites containing 10, 20, and 30 wt.% S53P4 were successfully synthesized via the sol-gel method, producing biphasic nanocomposites with high structural and elemental purity, as confirmed by FESEM analyses. The bioactivity evaluation in simulated body fluid (SBF) revealed that all composites induced the formation of an apatite layer after 21 days, with degradability and silicon ion release increasing proportionally with S53P4 content. MTT assays demonstrated that all formulations were cytocompatible, showing no significant toxicity to mammalian cells.
Additionally, FA contributed mild antibacterial activity through fluoride release, and increasing the S53P4 fraction enhanced antibacterial efficacy. Notably, the FA–BG–20 composite exhibited an optimal balance between antibacterial performance and cytocompatibility, suggesting it as the most promising formulation for bone tissue engineering applications where both infection prevention and cellular compatibility are critical. Overall, these results indicate that FA–BG nanocomposites combine controlled degradability, robust bioactivity, cytocompatibility, and antibacterial functionality, and that tuning the bioactive glass content allows for tailored scaffolds meeting both biological and mechanical requirements in bone regeneration applications.

Authors contributions
All authors contributed to the study conception and design. Material preparation, data collection and analysis were performed by Fatemeh mirjalili and sahebali manafi. The first draft of the manuscript was written by Fatemeh mirjalili and all authors commented on previous versions of the manuscript. All authors read and approved the final manuscript.

Availability of data and materials
The data that support the findings of this study are available from the corresponding author, upon reasonable request.

Conflict of interests
The authors declare that they have no known competing financial interests or personal relationships that could have appeared to influence the work reported in this paper.

References

Amaury Fau., Beyssac O., Gauthier M., Panczer G., Gasnault O. (2022) Timeresolved Raman and luminescence spectroscopy of synthetic REE-doped hydroxylapatites and natural apatites. *The American Mineralogist* 107:1341–1352.

Aoba T., Fejerskov O. (2002) Dental fluorosis: chemistry and biology. *Crit Rev Oral Biol Med* 13:155–70. DOI: https://doi.org/10.1177/154411130201300206.

Bigoni M., Turati M., Zanchi N., Lombardo A. S., Graci J., Omeljaniuk R. J., Zatti G., Gaddi D. (2019) Clinical applications of Bioactive glass S53P4 in bone infections: a systematic review. *Eur Rev Med Pharmacol Sci* 23:240–251. DOI: https://doi.org/10.26355/eurrev‘‘201904‘‘17498.

Borkowski L., Jojczuk M., Belcarz A., Pawlowska-Olszewska M., Kruk-Bachonko J., Radzki R., Bienko M., et al. (2023) Comparing the Healing Abilities of Fluorapatite and Hydroxyapatite Ceramics in Regenerating Bone Tissue: An *In Vivo* Study. *Materials (Basel)* 16:5992. DOI: https://doi.org/10.3390/ma16175992.

Brauer D. S. (2015) Bioactive glasses—structure and properties. *Angew Chem Int Ed* 54:4160–4181. DOI: https://doi.org/10.1002/anie.201405310.

Brudevold F., Gardner De., Smith Fa. (1956) The distribution of fluoride in human enamel. *J Dent Res* 35:420–9. DOI: https://doi.org/10.1177/00220345560350031301.

Buzalaf M. A. R., Pessan J. P., Honório H. M., Ten Cate J. M. (2011) Mechanisms of action of fluoride for caries control. *Monogr Oral Sci* 22:97–114. DOI: https://doi.org/10.1159/000325151.

Clarke B. (2008) Normal bone anatomy and physiology. *Clin J Am Soc Nephrol* 3:131–9. DOI: https://doi.org/10.2215/CJN.04151206.

Dorozhkin S. V. (2009) Calcium Orthophosphates in Nature, Biology and Medicine. *Materials* 32:399–498. DOI: https://doi.org/10.3390/ma2020399.

Drevet R., Fauré J., Benhayoune H. (2024) Electrophoretic Deposition of Bioactive Glass Coatings for Bone Implant Applications: A Review. *Coatings* 14:1084. https://doi.org/10.3390/coatings14091084

Elliott J. C. (2023) Structure and Chemistry of the Apatites and Other Calcium Orthophosphates. Elsevier Science

Elliott J. C., Mackie P. E., Young R. A. (1973) Monoclinic hydroxyapatite. *Science* 8 (10.1126/science.180.4090.1055): 1055–1057.

Featherstone J. D. (1999) Prevention and reversal of dental caries: role of low level fluoride. *Community Dent Oral Epidemiol* 27:31–40. DOI: https://doi.org/10.1111/j.1600-0528.1999.tb01989.x..

Feroz S., Khan S. (2020) Fluoride-substituted hydroxyapatite,Editor(s): Abdul Samad Khan, Aqif Anwar Chaudhry. Woodhead Publishing Series in Biomaterials, Handbook of Ionic Substituted Hydroxyapatites:175–196. DOI: https://doi.org/10.1016/B978-0-08-102834-6.00007-0.

Fleet M. E. (2009) Infrared spectra of carbonate apatites: ν_2-Region bands. *Biomaterials* 30:1473–1481. DOI: https://doi.org/10.1016/j.biomaterials.2008.12.007.

Florencio-Silva R., Sasso G. R., Sasso-Cerri E., Simões M. J., Cerri P. S. (2015) Biology of Bone Tissue: Structure, Function, and Factors That Influence Bone Cells. *Biomed Res* 2015:421746. DOI: https://doi.org/10.1155/2015/421746.

Gatti S. D., Gaddi D., Turati M., Leone G., Arts J. J., Pessina F., Carminati M., Zatti G., De Rosa L., Bigoni M. (2024) Clinical outcomes and complications of S53P4 bioactive glass in chronic osteomyelitis and septic non-unions: a retrospective single-center study. *Eur J Clin Microbiol Infect Dis* 43:489–499. DOI: https://doi.org/10.1007/s10096-023-04737-z.

Gerhardt L. C., Boccaccini A. R. (2010b) Bioactive Glass and Glass-Ceramic Scaffolds for Bone Tissue Engineering *Materials (Basel)* ——— (2010a) Bioactive Glass and Glass-Ceramic Scaffolds for Bone Tissue Engineering. *Materials (Basel, Switzerland)* 3:3867–3910. DOI: https://doi.org/10.3390/ma3073867.

Gorustovich A. A., Roether J. A., Boccaccini A. R. (2021) Effect of bioactive glasses on angiogenesis: a review of in vitro and in vivo evidences. *Tissue Eng Part B Rev* 16:199–207. DOI: https://doi.org/10.1089/ten.TEB.2009.0416.

Hench L. L., Wilson J. (2013) An Introduction to Bioceramics. 2nd ed. World Scientific DOI: https://doi.org/10.1142/P884.

Hoppe A., Güldal N. S., Boccaccini A. R. (2011) A review of the biological response to ionic dissolution products from bioactive glasses and glass-ceramics. *Biomaterials* 32:2757–74. DOI: https://doi.org/10.1016/j.biomaterials.2011.01.004.

Ielo I., Calabrese G., De Luca G., Conoci S. (2022) Recent Advances in Hydroxyapatite-Based Biocomposites for Bone Tissue Regeneration in Orthopedics. 27:9721. DOI: https://doi.org/10.3390/ijms23179721.

Jones J. R. (2013) Review of bioactive glass: From Hench to hybrids. *Acta Biomater* 9:4457–86. DOI: https://doi.org/10.1016/j.actbio.2012.08.023.

Kaou M. H., Furkó M., Balázsi K., Balázsi C. (2023a) Advanced Bioactive Glasses: The Newest Achievements and Breakthroughs in the Area. *Nanomaterials (Basel).* 9:2287. DOI: https://doi.org/10.3390/nano13162287.

——— (2023b) Advanced Bioactive Glasses: The Newest Achievements and Breakthroughs in the Area. *Nano Materials* 13:2287–232.

Kargozar S., Baino F., Hamzehlou S., Hill R. G., Mozafari M. (2018) Bioactive Glasses: Sprouting Angiogenesis in Tissue Engineering. *Trends Biotechnol.* 636:430–444. DOI: https://doi.org/10.1016/j.tibtech.2017.12.003.

Kaur G., Kumar V., Pickrell G. R., Mauro J. C., Lin Y., Arya S. K. (2019) Chapter 6 - Bioactive Glasses in Gene Regulation and Proliferation, Editor(s): Gurbinder Kaur,In Woodhead Publishing Series in Biomaterials,Biomedical, Therapeutic and Clinical Applications of Bioactive Glasses. Woodhead Publishing:175–200. DOI: https://doi.org/10.1016/B978-0-08-102196-5.00006-9.

Kazimierczak P., Wessely-Szponder J., Palka K., Barylyak A., Zinchenko V., Przekora A. (2023) Hydroxyapatite or Fluorapatite-Which Bioceramic Is Better as a Base for the Production of Bone Scaffold?-A Comprehensive Comparative Study. *International Journal of Molecular Sciences* 24:5576. DOI: https://doi.org/10.3390/ijms24065576.

Kokubo T., Takadama H. (2006) How useful is SBF in predicting in vivo bone bioactivity? *Biomaterials* 27:2907–2915. DOI: https://doi.org/10.1016/j.biomaterials.2006.01.017.

Kondo T., Otake K., Kakinuma H., Sato Y., Ambo S., Egusa H. (2024) Zinc- and Fluoride-Releasing Bioactive Glass as a Novel Bone Substitute. *Journal of Dental Research* 103:526–535. DOI: https://doi.org/10.1177/00220345241231772.

LeGeros R. Z. (2002) Properties of osteoconductive biomaterials: calcium phosphates. *Clin Orthop Relat Res* 395:81–98. DOI: https://doi.org/10.1097/00003086-200202000-00009.

Lindfors N., Geurts J., Drago L., Arts J. J., Juutilainen V., Hyvönen P., Suda A. J., et al. (2017) Antibacterial Bioactive Glass, S53P4, for Chronic Bone Infections - A Multinational Study. *Adv Exp Med Biol* 971 (10.1007/5584_2016_156): 81–92.

Madupalli H., Pavan B., Tecklenburg M. M. J. (2017) Carbonate substitution in the mineral component of bone: Discriminating the structural changes, simultaneously imposed by carbonate in A and B sites of apatite. *J Solid State Chem* 225:27–35. DOI: https://doi.org/10.1016/j.jssc.2017.07.025.

Manafi S., Mirjalili F., Hajisafari M., Orand F. (2019a) Preparation and characterization of fluorapatite-bioactive glass S53P4 nanocomposite. *J Nanoanalysis* 6:145–56. http://creativecommons.org/licenses/by/4.0/

Manafi S., Mirjalili F., Reshadi R. (2019b) Synthesis and evaluation of the bioactivity of fluorapatite–45S5 bioactive glass nanocomposite. *Prog Biomater* 8:77–9.
DOI: https://doi.org/10.1007/s40204-019-0112-y.

Montazerian M., Baino F., Fiume E., Migneco C. (2022) Glass-ceramics in dentistry: Fundamentals, technologies, experimental techniques, applications, and open issues. *Progress in Materials Science* 132:101023. DOI: https://doi.org/10.1016/j.pmatsci.2022.101023.

Nielson C., JAgarwal J., Peter Beck J., Shea J., Jeyapalina S. (2024) Sintered fluorapatite scaffolds as an autograft-like engineered bone graft. *Journal of Bio Medical Materials Research* 112:35374.
DOI: https://doi.org/10.1002/jbm.b.35374.

Pandayil J. T., Boetti N. G., Janner D. (2024) Advancements in Biomedical Applications of Calcium Phosphate Glass and Glass-Based Devices-A Review. *J Funct Biomater* 21:79.
DOI: https://doi.org/10.3390/jfb15030079.

Rahaman M. N., Day D. E., Bal B. S., Fu Q., Jung S. B., Bonewald L. F., Tomsia A. P. (2011) Bioactive glass in tissue engineering. Acta Biomater:2355–73.
DOI: https://doi.org/10.1016/j.actbio.2011.03.016.

Rahaman M. N., Mao J. J. (2005) Stem cell-based composite tissue constructs for regenerative medicine. *Biotechnol Bioeng* 91:261–84.
DOI: https://doi.org/10.1002/bit.20292.

Rezwan K., Chen Q. Z., Blaker J. J., Boccaccini A. R. (2006) Biodegradable and bioactive porous polymer/inorganic composite scaffolds for bone tissue engineering. *Biomaterials* 27:3413–31.
DOI: https://doi.org/10.1016/j.biomaterials.2006.01.039.

Santiago E., Martin V., Colaço B., Fernandes M. H., Santos C., Gomes P. S. (2022) Hydrothermal Synthesis of Fluorapatite Coatings over Titanium Implants for Enhanced Osseointegration-An *In Vivo* Study in the Rabbit. *J Funct Biomater* 14:241.
DOI: https://doi.org/10.3390/jfb13040241.

Seyedmajidi S., Rajabnia R., Seyedmajidi M. (2018) Evaluation of antibacterial properties of hydroxyapatite/bioactive glass and fluorapatite/bioactive glass nanocomposite foams as a cellular scaffold of bone tissue. *J Lab Physicians* 10:265–270.
DOI: https://doi.org/10.4103/JLP.JLP‟¨167“¨7.

Seyedmajidi S., Seyedmajidi M., Haghanifar S. (2023) Optimization of Fluorapatite/Bioactive Glass Nanocomposite Foams as Bone Tissue Scaffold: An *in Vivo* Study. *Int J Mol Cell Med* 12:388–400.
DOI: https://doi.org/10.22088/IJMCM.BUMS.12.4.388.

Shearer A., Montazerian M., Sl J. J., Hill R. G., Mauro J. C. (2023) Trends and perspectives on the commercialization of bioactive glasses. *Acta biomaterialia* 160:14–31.
DOI: https://doi.org/10.1016/j.actbio.2023.02.020.

Ten Cate J. M. (1999) Current concepts on the theories of the mechanism of action of fluoride. *Acta Odontol Scand* 57:325–9.
DOI: https://doi.org/10.1080/000163599428562.

Vallet-Regí M., Colilla M., Izquierdo-Barba I., Vitale-Brovarone C., Fiorilli S. (2022) Achievements in Mesoporous Bioactive Glasses for Biomedical Applications. *Pharmaceutics* 14:2636–2646.
DOI: https://doi.org/10.3390/pharmaceutics14122636.

van Gestel N. A., Geurts J., Hulsen D. J., van Rietbergen B., Hofmann S., Arts J. J. (2015) Clinical Applications of S53P4 Bioactive Glass in Bone Healing and Osteomyelitic Treatment: A Literature Review. *Biomed Res Int.* 2015:684826.
DOI: https://doi.org/10.1155/2015/684826.

Välimäki V. V., Aro H. T. (2006) Molecular basis for action of bioactive glasses as bone graft substitute. *Scand J Surg* 95:95–102.
DOI: https://doi.org/10.1177/145749690609500204.

Weatherell J. A., Strong M., Robinson C., Ralph J. P. (1986) Fluoride distribution in the mouth after fluoride rinsing. *Caries Res* 20:111–9.
DOI: https://doi.org/10.1159/000260929.

Weatherell JA Robinson C Ralph JP Strong M (1986) Fluoride distribution in the mouth after fluoride rinsing. *Caries Res* 20:111–9.
DOI: https://doi.org/10.1159/000260929.

Xuan B., Quynh Huong D., Thu Thu T., Ngoc Nghia N. (2024) Systematic Review of Study on the Clinical Effectiveness of Bioactive Glass S53P4 in the Treatment of Osteomyelitis. *VNU Journal of Science: Medical and Pharmaceutical Sciences* 40:25–33.
DOI: https://doi.org/10.25073/2588-1132/vnumps.4686.

Xynos I. D., Edgar A. J., Buttery L. D., Hench L. L., Polak J. M. (2001) Gene-expression profiling of human osteoblasts following treatment with the ionic products of Bioglass 45S5 dissolution. *J Biomed Mater Res* 55:151–157.
DOI: https://doi.org/10.1002/1097-4636(200105)55:2.

——— (2000) Ionic products of bioactive glass dissolution increase proliferation of human osteoblasts and induce insulin-like growth factor II mRNA expression and protein synthesis. *Biochem Biophys Res Commun* 276:461–5. DOI: https://doi.org/10.1006/bbrc.2000.3503.

Ylänen H. (2017) Bioactive Glasses Materials, Properties and Applications. Woodhead DOI: https://doi.org/10.1016/C2015-0-05462-4.

Zhao D. (2008) Mechanical verification of soft- tissue attachment on bioactive glasses and titanium implants. *Acta Biomaterial* 4 (10.1016/j.actbio.2008.02.012): 1118–1122.

Zhou H., Lee J. (2011) Nanoscale hydroxyapatite particles for bone tissue engineering. *Acta Biomaterialia, volume = 7, doi=10.1016/j.actbio.2011.03.019, pages = 2769-2781*